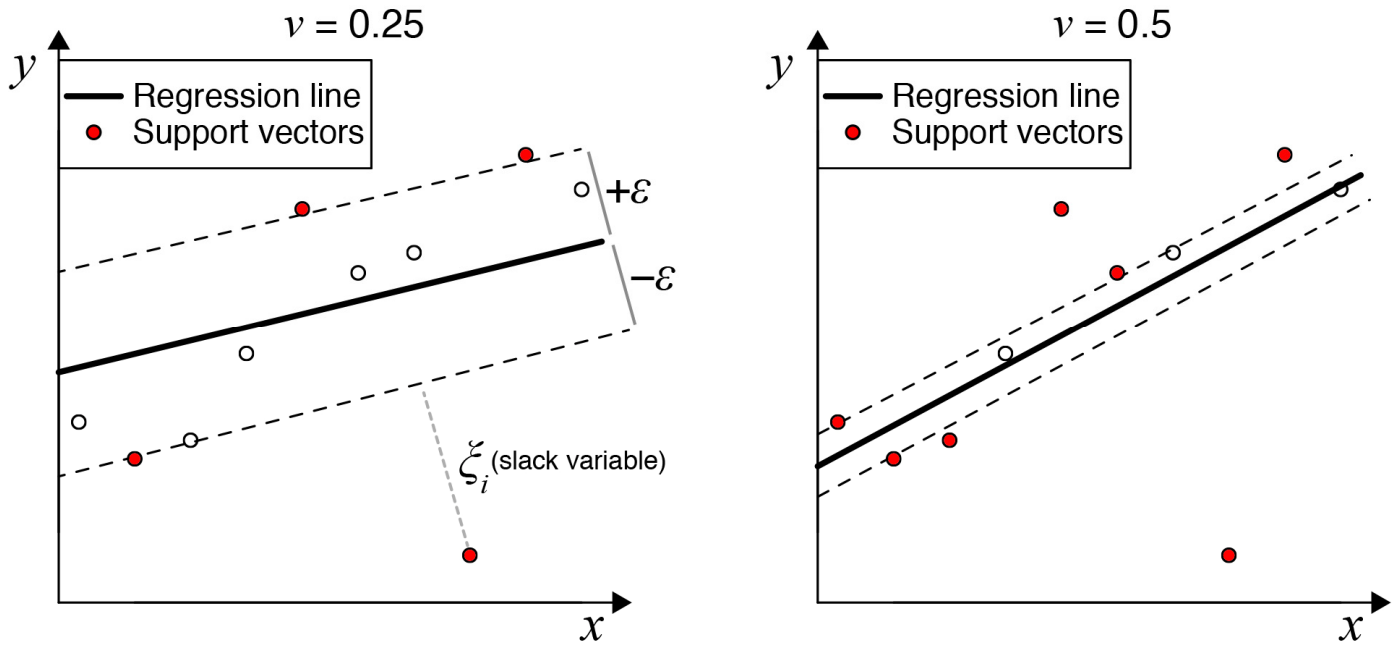

Supplementary Figure 1

Illustrative example of support vector regression

A simple two-dimensional dataset analyzed with linear *v*-SVR, with results shown for two values of *v* (note that both panels show the same data points). As detailed in Online Methods, linear SVR identifies a hyperplane (which, in this two-dimensional example, is a line) that fits as many data points as possible (given its objective function) within a constant distance, *ε* (open circles). Data points lying outside of this '*ε*-tube' are termed 'support vectors' (red circles), and are penalized according to their distance from the *ε*-tube by linear slack variables (ξ_i). Importantly, the support vectors alone are sufficient to completely specify the linear function, and provide a sparse solution to the regression that reduces the chance of overfitting. In *v*-SVR, the *v* parameter determines both the lower bound of support vectors and upper bound of training errors. As such, higher values of *v* result in a smaller *ε*-tube and a greater number of support vectors (right panel). For CIBERSORT, the support vectors represent genes selected from the signature matrix for analysis of a given mixture sample, and the orientation of the regression hyperplane determines the estimated cell type proportions in the mixture. For further details, including the key technical advantages of *v*-SVR for GEP deconvolution, see Online Methods.

Reference (Main Text)

10. Schölkopf, B., Smola, A.J., Williamson, R.C. & Bartlett, P.L. *Neural Comput*. **12**, 1207-1245 (2000).

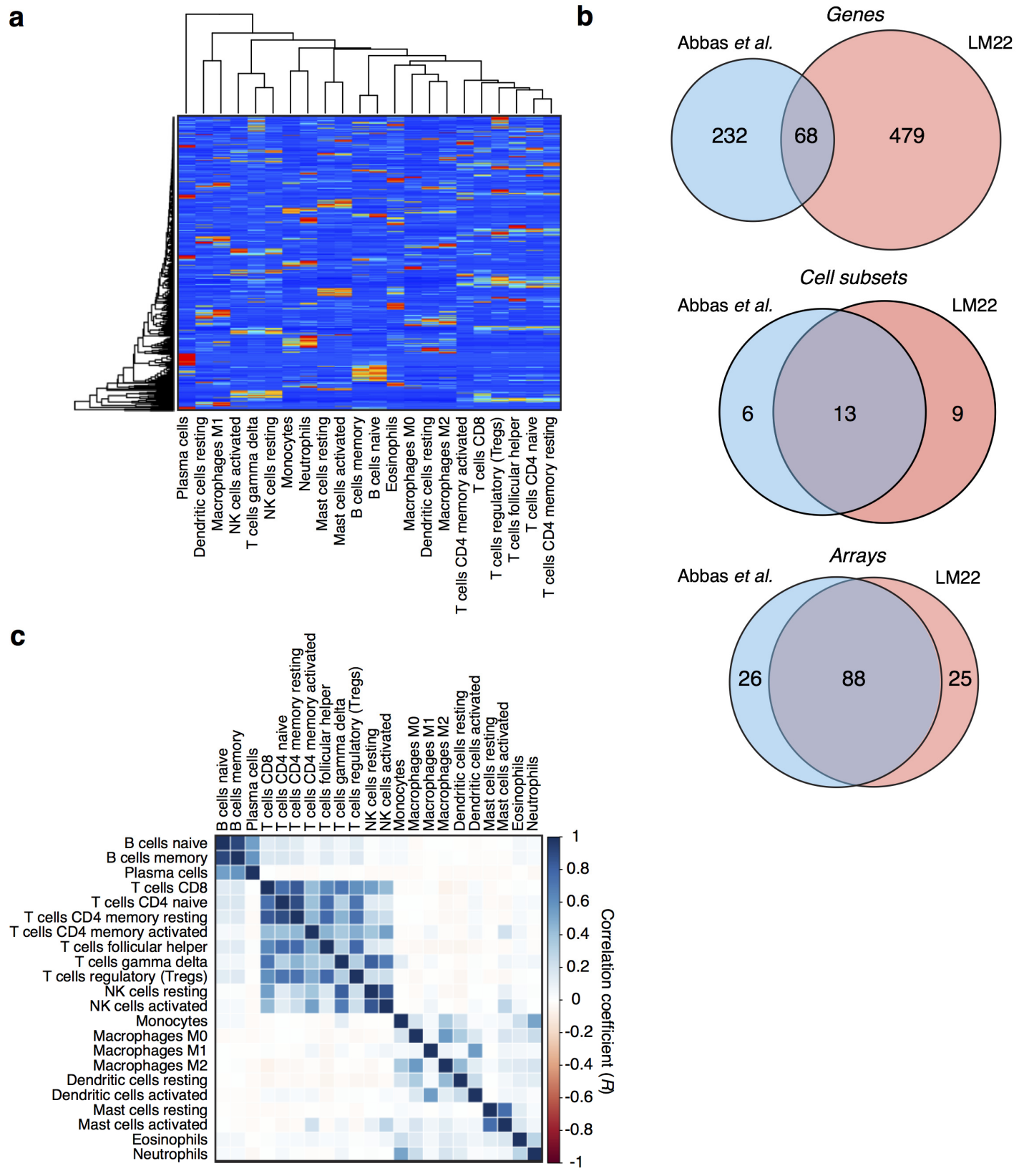

Supplementary Figure 2

LM22 signature matrix and comparison to Abbas *et al*.

(**a**) Heat map of the LM22 signature matrix (**Supplementary Table 1**) depicting the relative expression of each gene across 22 leukocyte subsets. Gene expression levels were unit variance normalized, and cell subsets and genes were clustered hierarchically using Euclidean distance (higher expression, red; lower expression, blue). (**b**) Overlap between LM22 and a previously published signature matrix (GSE22886) with respect to genes, cell subsets, and expression arrays used. For gene overlap between Abbas *et al*. and LM22, we considered all Affymetrix probesets as 'genes', including those not resolvable to HUGO gene symbols (n = 36). For cell subset overlap, we only considered cell types profiled in GSE22886; this dataset contains 22 distinct phenotypes, and six were pooled into three phenotypes for incorporation into LM22, resulting in an overlap of 13 (for details, see **Supplementary Table 1**). (**c**) All-versus-all heat map of correlation coefficients (Pearson) comparing the reference profiles of each cell subset in LM22 (genes were normalized as described in Methods; same as **Supplementary Table 1**).

Reference (Main Text)

4. Abbas, A.R., Wolslegel, K., Seshasayee, D., Modrusan, Z. & Clark, H.F. *PLoS One* **4**, e6098 (2009).

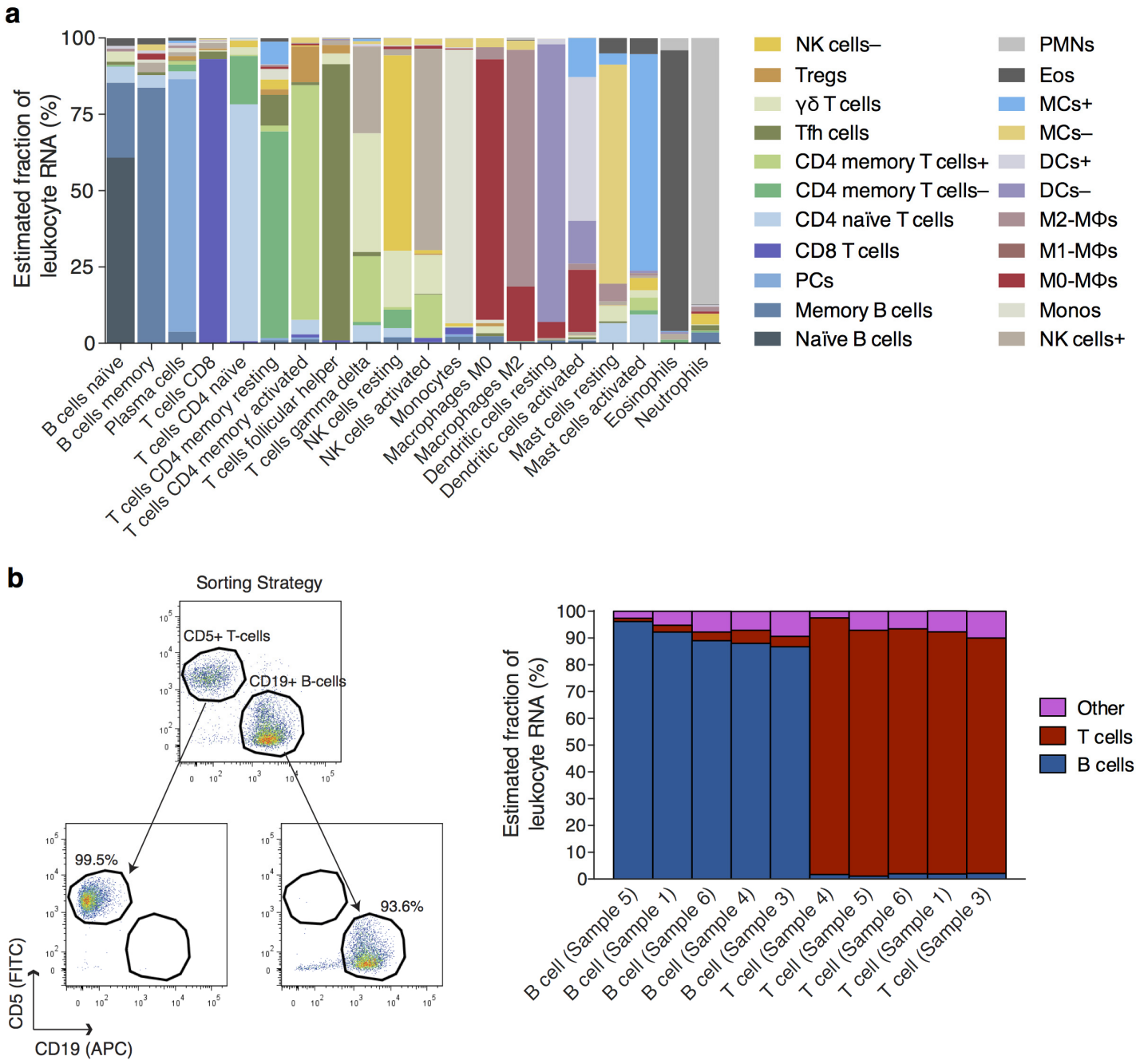

Supplementary Figure 3

Validation of LM22 by analysis of purified leukocyte subsets

(**a**) Fractions of each LM22 cell subset called by CIBERSORT in validation arrays containing purified/enriched leukocytes profiled in LM22 (related to **Fig. 1b**; also see **Supplementary Table 2**). Results for arrays of a given cell subset are summarized as median fractions. Cell subset abbreviations in the color key are defined in **Supplementary Table 1**. (**b**) Left: B and T lymphocytes were flow-sorted from five human tonsils to mean purity levels exceeding 95% and 98%, respectively, and then profiled by microarray. Right: The fractional representations of these B/T cells, along with any remaining leukocyte content, as inferred by CIBERSORT.

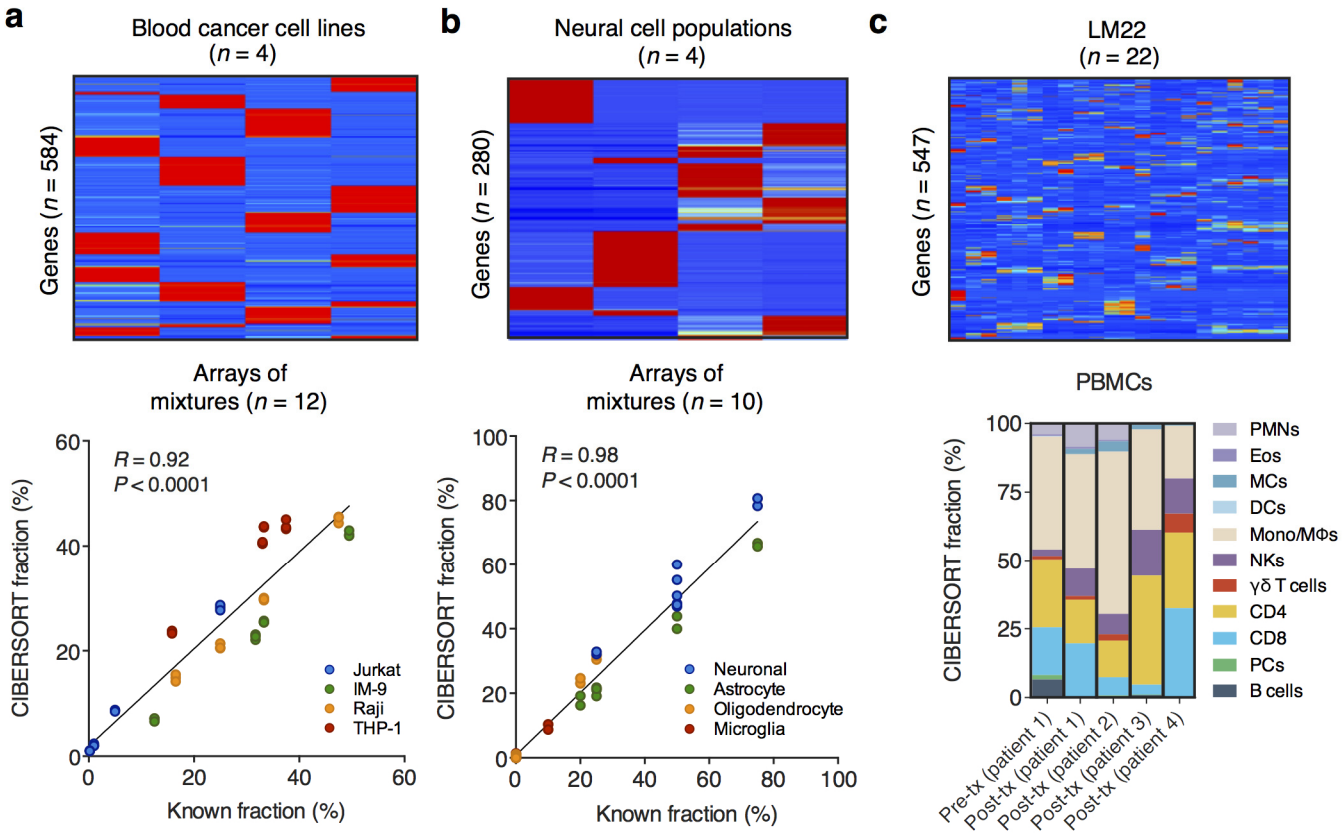

Supplementary Figure 4

Resolution of well-defined mixtures with CIBERSORT

Analysis of CIBERSORT performance using different signature matrices (top) applied to different mixtures (bottom). Top: Cell population reference expression signatures for (**a**) purified blood cancer cell line expression profiles in GSE11103, (**b**) neural gene expression profiles in GSE19380, and (**c**) LM22 (**Supplementary Table 1**). Bottom: Comparison of known and inferred fractions for defined mixtures of (**a**) blood cancer cell lines (GSE11103) and (**b**) neural cell types (GSE19380). Concordance was assessed by Pearson correlation (*R*) and linear regression (solid lines). (**c**) CIBERSORT analysis of pre- and post-Rituximab therapy PBMC samples, including one paired sample, from four Non-Hodgkin's lymphoma patients using LM22 (pooled into 11 leukocyte types for clarity; see **Supplementary Table 1**).

References (Main Text)

4. Abbas, A.R., Wolslegel, K., Seshasayee, D., Modrusan, Z. & Clark, H.F. *PLoS One* **4**, e6098 (2009).

13. Kuhn, A., Thu, D., Waldvogel, H.J., Faull, R.L.M. & Luthi-Carter, R. *Nat. Methods* **8**, 945-947 (2011).

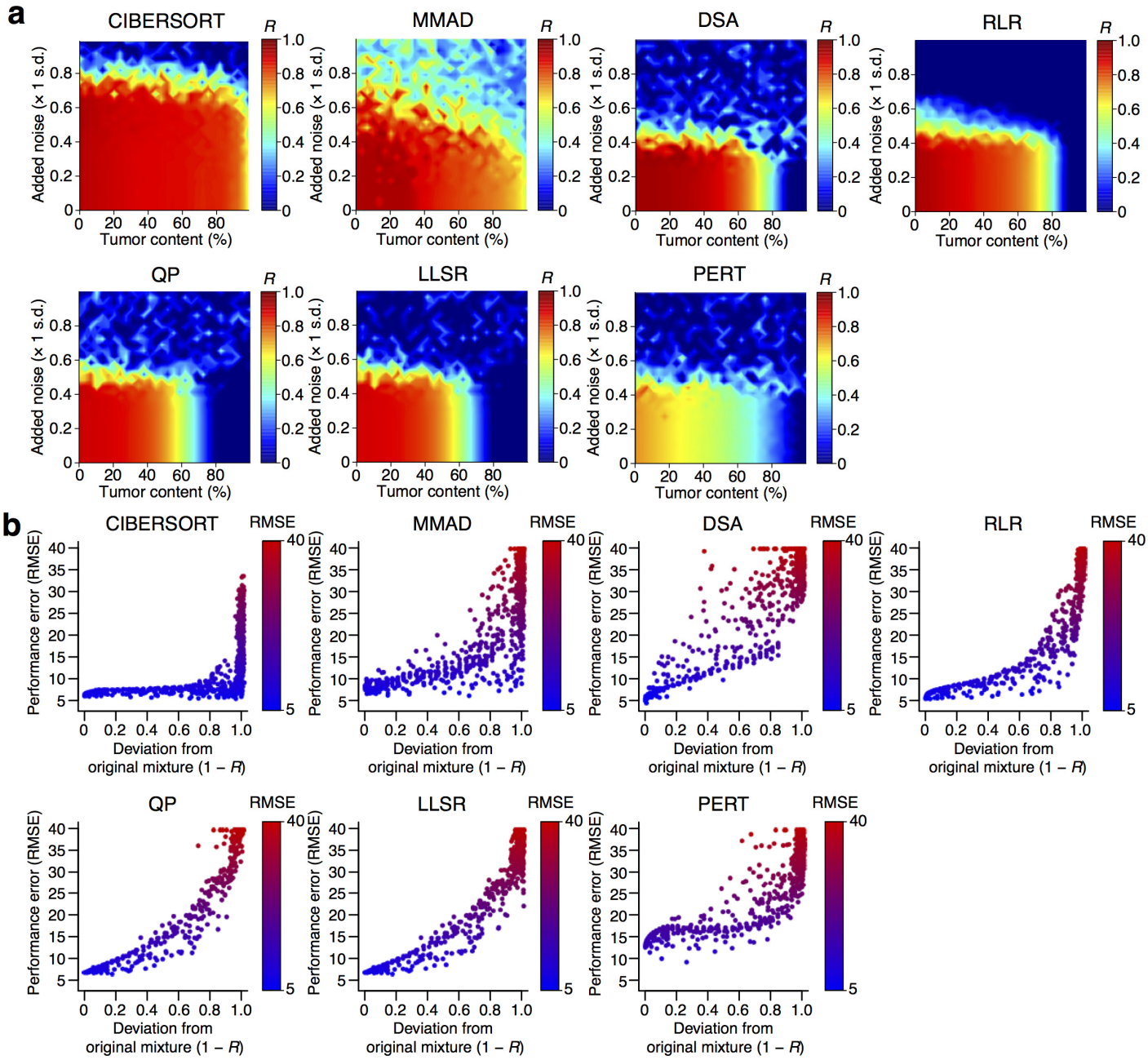

Supplementary Figure 5

Comparative analysis of deconvolution methods on simulated tumors with added noise

(**a**, **b**) Performance of each method with respect to added tumor content (*x*-axis) and non-log linear noise (*y*-axis) (see Online Methods for details). Each parameter was analyzed in evenly spaced intervals for a total of 900 mixtures (30 x 30). (**a**) Concordance between known and estimated cell type proportions as determined by Pearson correlation coefficient (*R*), with a floor of zero. (**b**) Performance evaluated as a function of the deviation of each mixture from its original, unmodified values (represented on the *x*-axis as 1 – *R*). Differences between known and predicted cell type proportions (represented as percentages) in **b** were assessed by root mean squared error (RMSE), with a ceiling of 40.

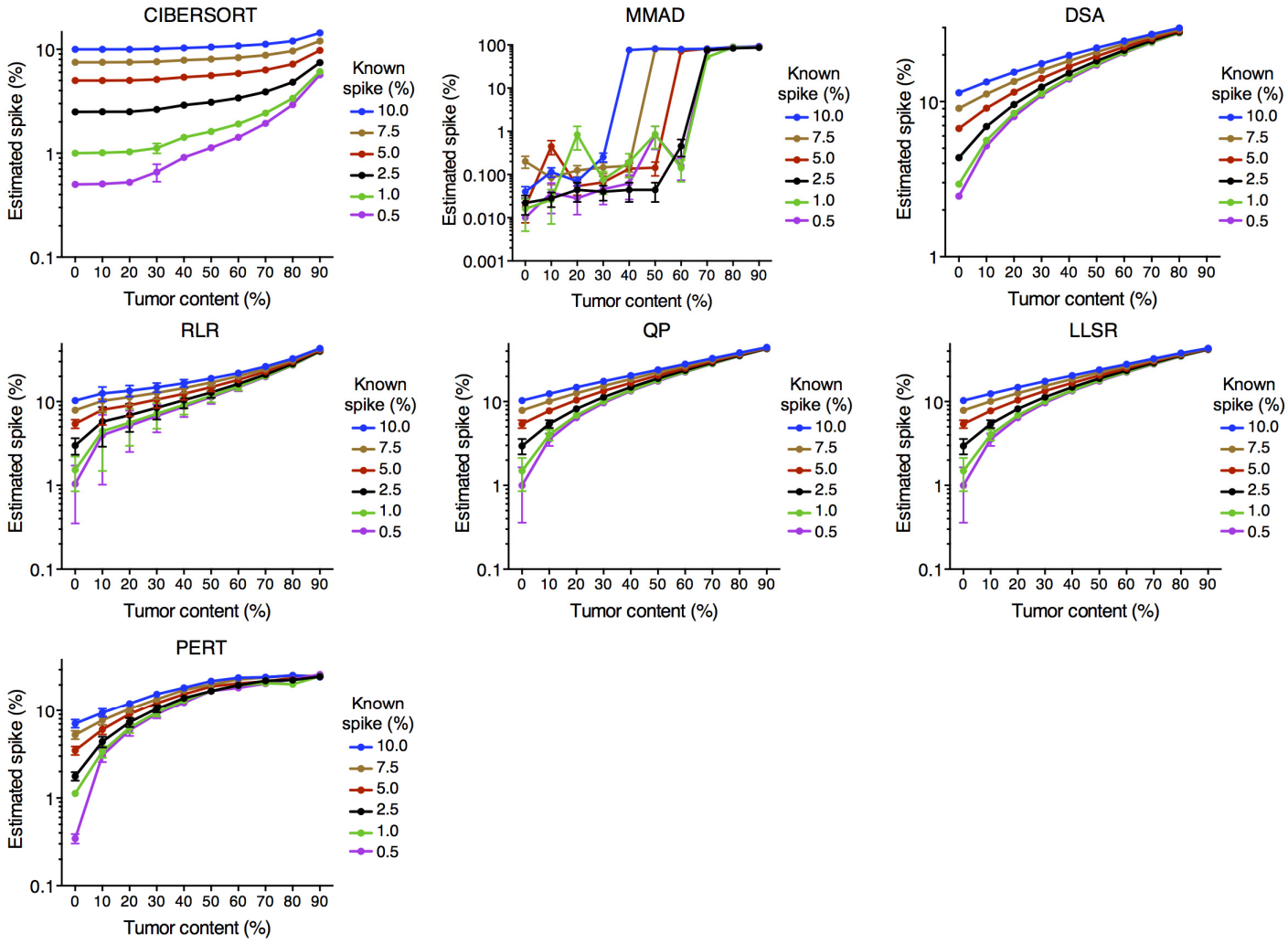

Supplementary Figure 6

Comparison of deconvolution methods with respect to detection limit in simulated mixtures with unknown content

Each color represents a defined input concentration for a given cell type (here, Jurkat), and each line represents its concentration as predicted by GEP deconvolution. Known Jurkat concentrations were measured across a range of added tumor content in five simulated mixtures of four blood cell lines, with different concentrations of a colon cancer line (see Online Methods). Data are presented as medians (n = 5 mixtures) ± 95% confidence intervals.

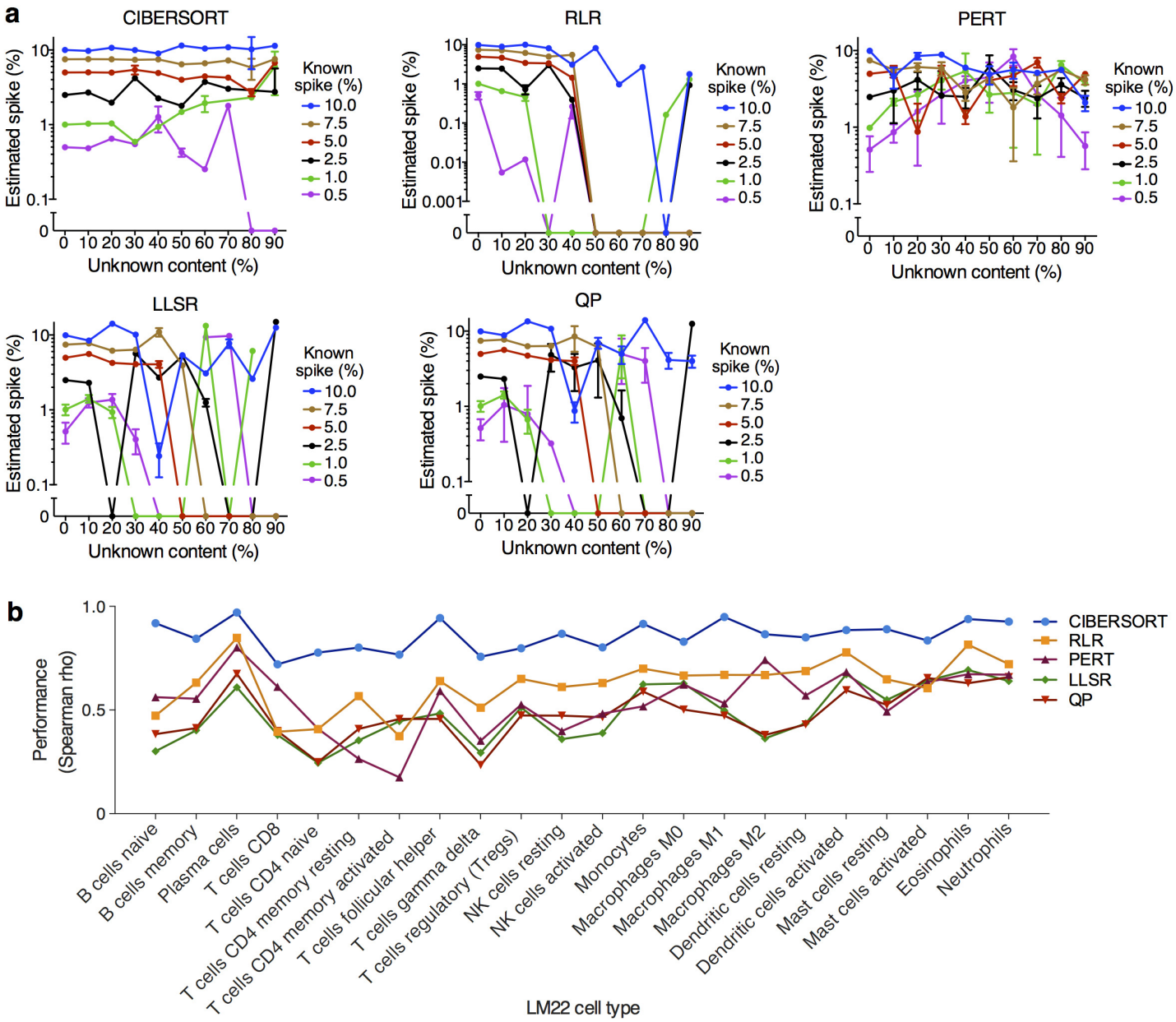

Supplementary Figure 7

Analysis of detection limit for each cell subset in LM22

(**a**) Same as in **Supplementary Fig. 6**, except here detection limit was assessed using defined inputs of naïve B-cells added to simulated mixtures of the remaining 21 cell types from LM22 (**Supplementary Table 1**). The impact of unknown content on detection limit was evaluated by adding simulated GEPs created by randomly permuting naïve B-cell genes. Data are presented as medians (n = 4 mixtures) ± 95% confidence intervals. (**b**) Same as in **a**, but for all cell types in LM22. To prevent higher magnitude spike-ins from driving the correlation, we summarized performance using the non-parametric Spearman rank correlation, and compared known and predicted fractions over all spike-ins and levels of unknown content tested. Considering these results in aggregate, CIBERSORT significantly outperformed other methods tested (P < 0.0001; paired two-sided Wilcoxon signed rank test; n = 22 cell subsets). Of note, CIBERSORT also outperformed other methods in relation to linear fit, as measured by Pearson correlation. For further details, see Online Methods.

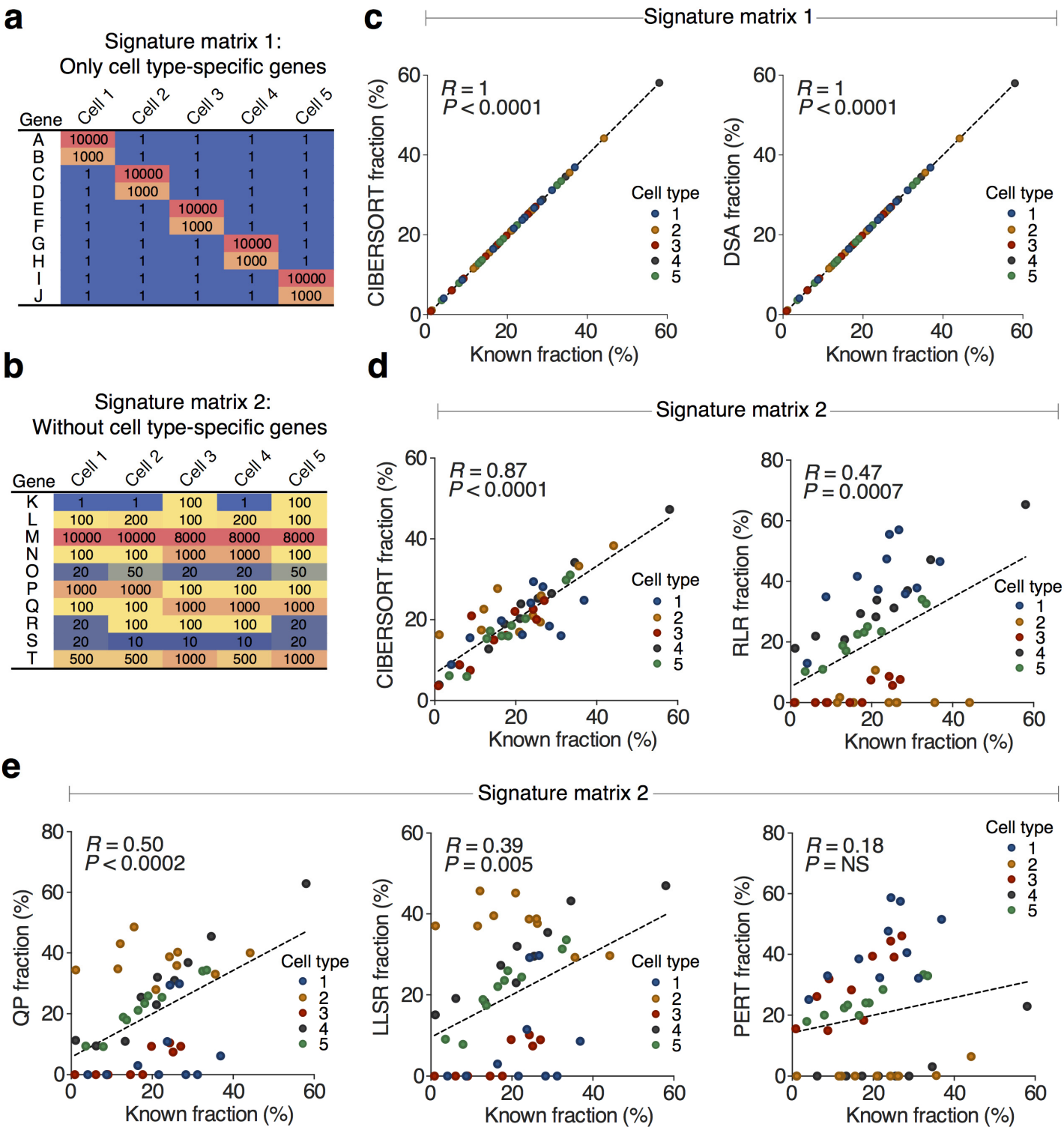

Supplementary Figure 8

Impact of marker genes on deconvolution

(**a**) Heat map of signature matrix 1 (SM1), which contains only cell type specific marker genes. (**b**) Heat map of signature matrix 2 (SM2), which contains only non-cell type specific marker genes. (**c**) CIBERSORT and DSA deconvolution performance on ten mixtures

created using SM1. (**d**,**e**) Deconvolution performance on ten mixtures created using SM2: (**d**) CIBERSORT and RLR, (**e**) QP, LLSR, and PERT. For details, see Online Methods. Statistical concordance between known and observed cell type proportions was determined by linear regression (dashed lines) and Pearson correlation (*R*).

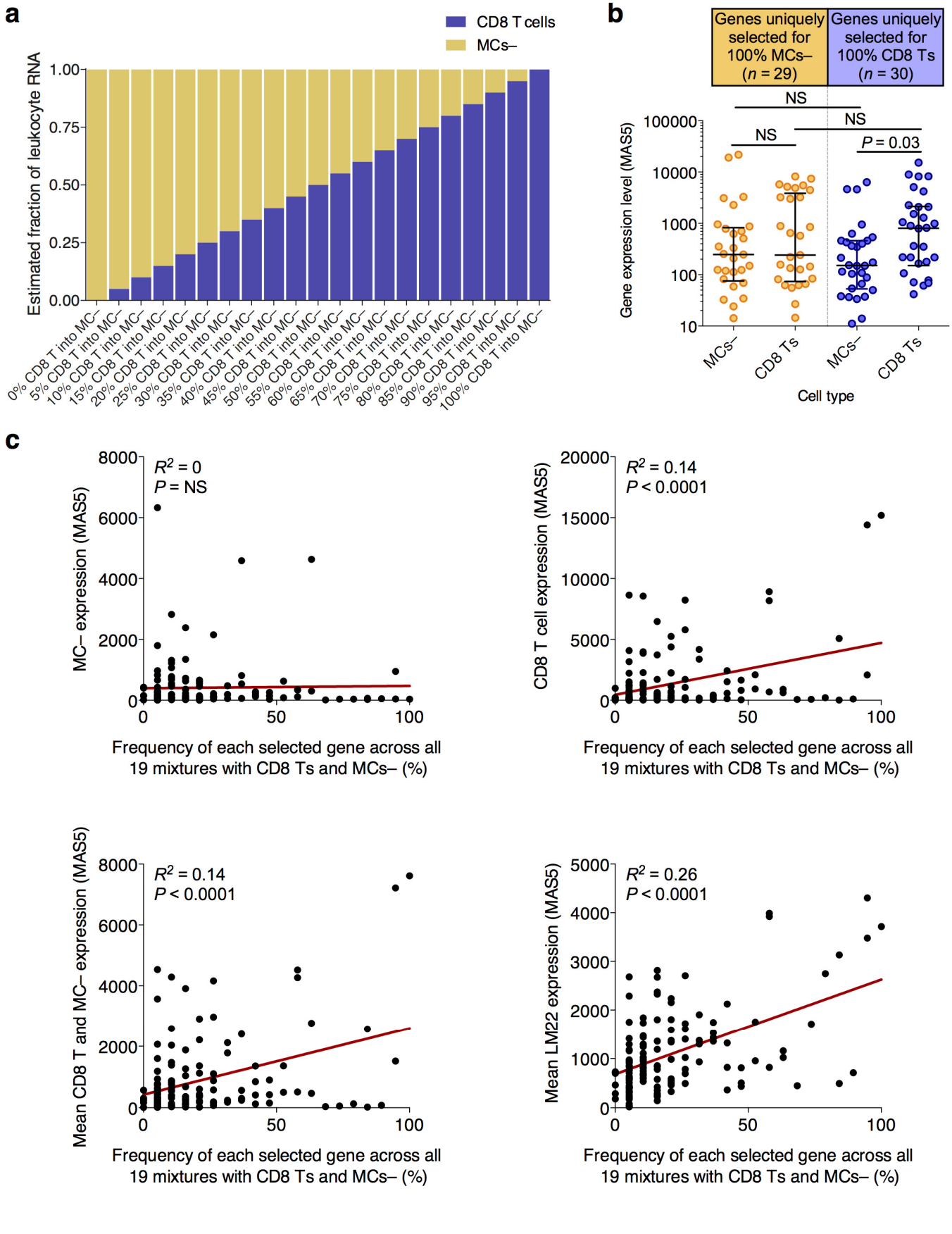
a
CD8 T cells
MCs–
Estimated fraction of leukocyte RNA
1.00
0.75
0.50
0.25
0.00
0% CD8 T into MC–
5% CD8 T into MC–
10% CD8 T into MC–
15% CD8 T into MC–
20% CD8 T into MC–
25% CD8 T into MC–
30% CD8 T into MC–
35% CD8 T into MC–
40% CD8 T into MC–
45% CD8 T into MC–
50% CD8 T into MC–
55% CD8 T into MC–
60% CD8 T into MC–
65% CD8 T into MC–
70% CD8 T into MC–
75% CD8 T into MC–
80% CD8 T into MC–
85% CD8 T into MC–
90% CD8 T into MC–
95% CD8 T into MC–
100% CD8 T into MC–
b
Genes uniquely selected for 100% MCs– (n = 29)
Genes uniquely selected for 100% CD8 Ts (n = 30)
NS
NS
NS
P = 0.03
Gene expression level (MAS5)
100000
10000
1000
100
10
MCs–
CD8 Ts
MCs–
CD8 Ts
Cell type
c
R2 = 0
P = NS
MC– expression (MAS5)
8000
6000
4000
2000
0
0
50
100
Frequency of each selected gene across all 19 mixtures with CD8 Ts and MCs– (%)
R2 = 0.14
P < 0.0001
CD8 T cell expression (MAS5)
20000
15000
10000
5000
0
0
50
100
Frequency of each selected gene across all 19 mixtures with CD8 Ts and MCs– (%)
R2 = 0.14
P < 0.0001
Mean CD8 T and MC– expression (MAS5)
8000
6000
4000
2000
0
0
50
100
Frequency of each selected gene across all 19 mixtures with CD8 Ts and MCs– (%)
R2 = 0.26
P < 0.0001
Mean LM22 expression (MAS5)
5000
4000
3000
2000
1000
0
0
50
100
Frequency of each selected gene across all 19 mixtures with CD8 Ts and MCs– (%)

Supplementary Figure 9

Analysis of feature (gene) selection in defined mixtures

(**a**) Results from applying CIBERSORT to a spike series, in which the LM22 reference profile for CD8 T cells was spiked into the corresponding reference profile for resting mast cells (MCs–) in even increments (*n* = 21). (Of note, both cell types have highly distinct expression vectors in LM22; see **Supplementary Fig. 2c**.) (**b**) Comparison between genes selected by support vector regression (SVR) to deconvolve 100% resting mast cells, but not CD8 T cells, and vice versa. For each unique subset of genes, expression levels in the LM22 signature matrix are further compared between resting mast cells and CD8 T cells. A paired two-sided Wilcoxon signed rank test was used for within group comparison and an unpaired two-sided Wilcoxon rank sum test was used for between group comparisons. Data are presented as medians ± interquartile range. While genes uniquely selected for the 100% CD8 T cell sample are significantly more expressed in CD8 T cells than resting mast cells, the magnitude is small. Moreover, the opposite scenario is not observed for resting mast cell genes in the 100% resting mast cell sample, suggesting SVR gene selection is not strongly correlated with the presence or absence of a particular cell subset in the mixture. (**c**) Comparison between gene expression levels in LM22 (*n* = 547 genes) and the frequency that each gene was selected, if at all, by SVR from the set of 19 mixtures with >0% CD8 T cells and >0% resting mast cells (see panel **a**). Top: Comparison with expression levels of (left) CD8 T cells or (right) resting mast cells. Bottom: Comparison with mean expression levels of (left) CD8 T cells and resting mast cells or (right) all cell subsets in LM22. Regardless of spike-in composition, the highest correlation between expression and gene selection frequency was observed when considering all cell types in LM22. Statistical concordance in **c** was determined by linear regression (red lines).

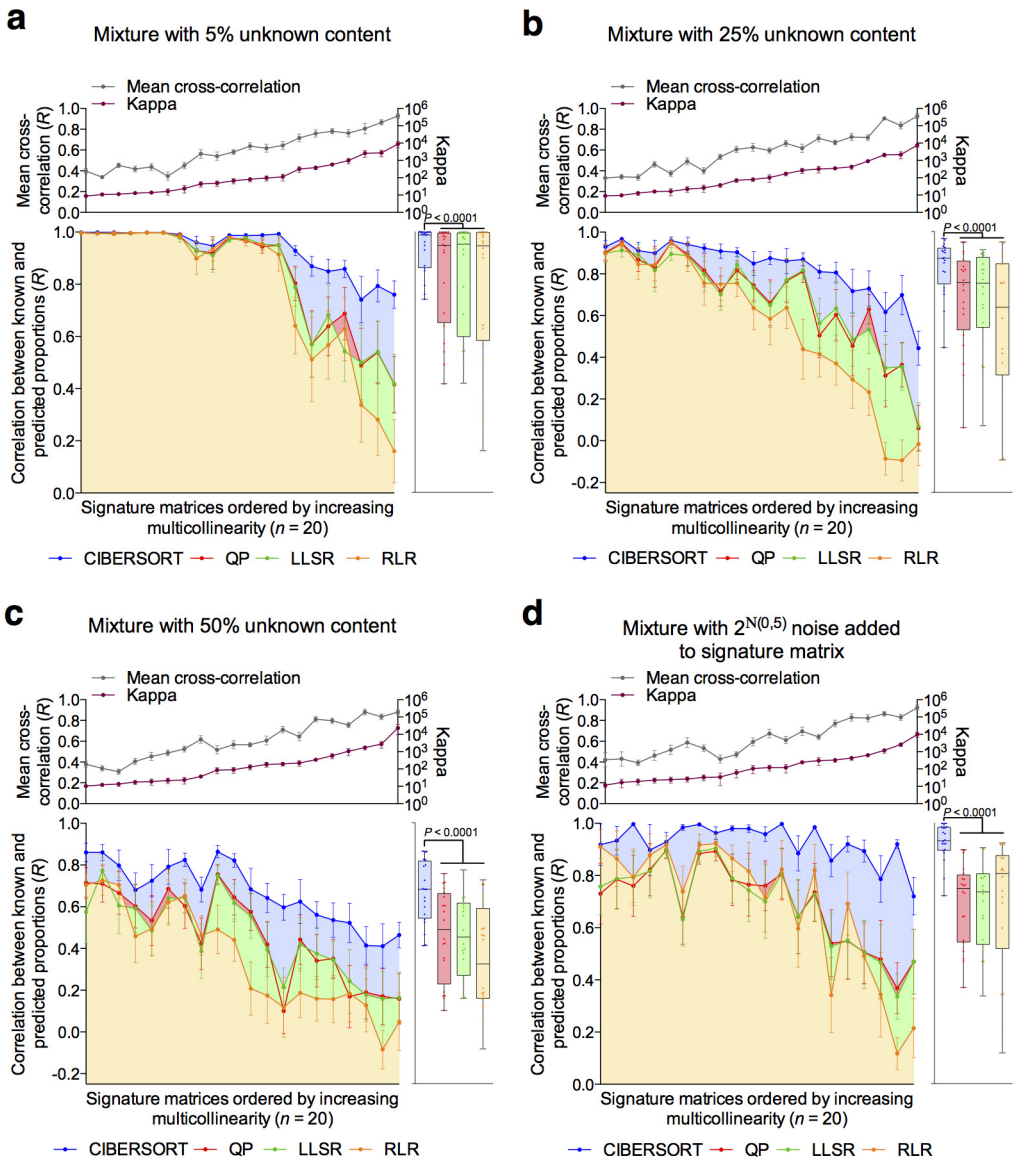

Supplementary Figure 10

Impact of multicollinearity on signature matrix–based methods

(**a**–**d**) The effect of multicollinearity on deconvolution performance is shown for mixtures with unknown content (**a**-**c**) or noise added to the signature matrix (**d**). Each panel is organized as follows: Top: The mean cross-correlation coefficient (left *y*-axis) and corresponding mean condition number kappa (right *y*-axis) of signature matrix GEPs over a broad range of multicollinearity values (*x*-axis; Online Methods). 'Mean cross correlation' indicates the average value of an all-versus-all correlation comparison (Pearson) of signature matrix reference profiles, whereas 'kappa' is a measure of signature matrix stability (Online Methods). Both metrics capture multicollinearity (or the degree of similarity among reference profiles) in the signature matrix. Bottom left: The relative performance of four deconvolution methods on simulated mixtures, comparing known and predicted cellular fractions (*y*-axis). Results from 20 levels of multicollinearity are shown ordered by increasing multicollinearity (left to right). Each level of multicollinearity was simulated ten times, and summarized values are presented as means ± s.e.m. Bottom right: Summarization of the performance of each method as a box plot, with interquartile range contained in the box and minimum and maximum points denoted by whiskers. Group comparisons between CIBERSORT and other methods were performed using a paired two-sided Wilcoxon signed rank test. All signature matrices and mixture vectors were unit variance normalized prior to analysis. For additional details, see Online Methods.

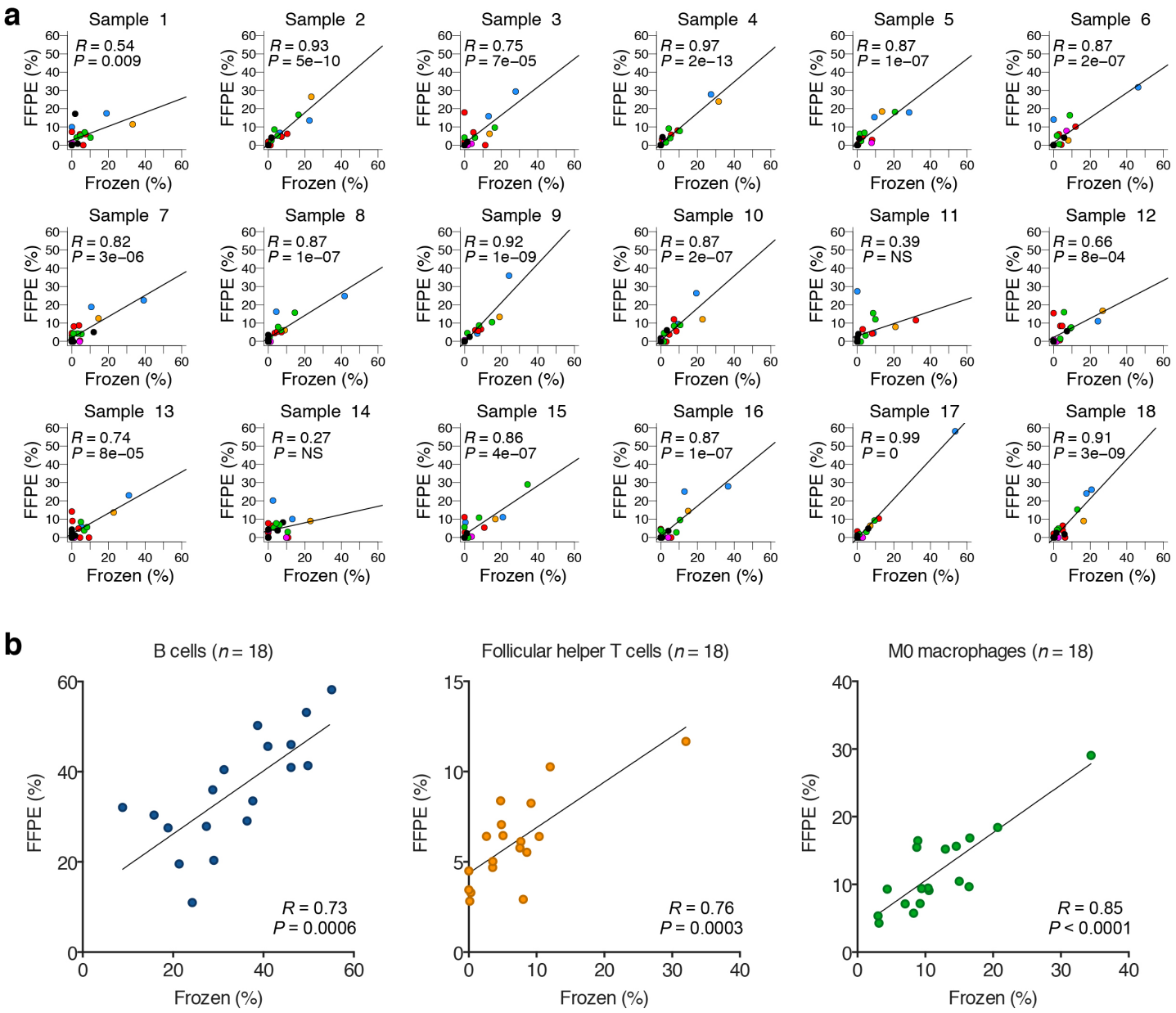

Supplementary Figure 11

Comparison of leukocyte deconvolution results between frozen and FFPE samples in 18 individual DLBCL tumors

(**a**) Results are shown for the 22 leukocyte subsets resolved in each tumor, related to **Fig. 2g**. Data points (circles) are colored as in **Fig. 2g** and indicate cell type. Deconvolution results for sample IDs 11 and 14 were not significantly correlated between FFPE and frozen conditions (NS). (**b**) Scatter plots for representative cell types across all 18 tumors. Expression data were obtained from GSE18377. Linear regression (solid lines) was used to compare all paired data in **a**, **b**. *R*, Pearson correlation.

Reference (Main Text)

16. Burington, B. et al. *Sci. Transl. Med*. **3**, 74ra22 (2011).

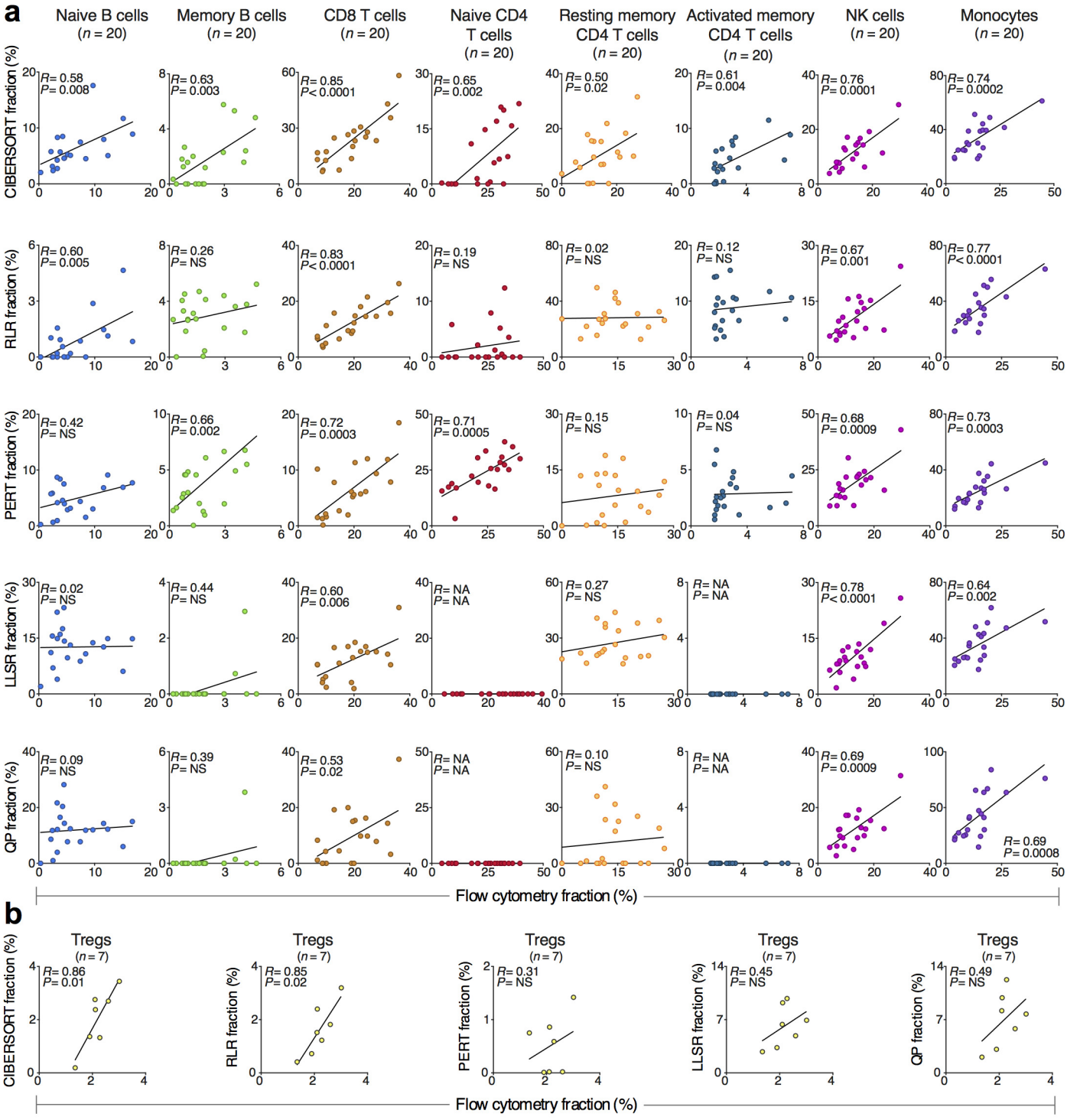

Supplementary Figure 12

Comparison of deconvolution methods for enumeration of nine leukocyte subsets in PBMCs

(**a**) Scatter plots comparing flow cytometry with five deconvolution methods for the enumeration of eight leukocyte subsets in 20 PBMC samples. (**b**) Same as in **a** but for Tregs, which were exclusively profiled in a separate cohort of seven PBMC samples. Of ten total phenotypic subsets analyzed in PBMCs (Online Methods), the nine subsets shown here were deconvolved by at least one method with a correlation coefficient of at least 0.5 (only gamma delta T cells are not shown). Detailed performance metrics for all ten subsets are

provided in **Supplementary Table 4**. Linear regression (solid lines) was used to statistically compare all paired data in **a**, **b**. *R*, Pearson correlation.

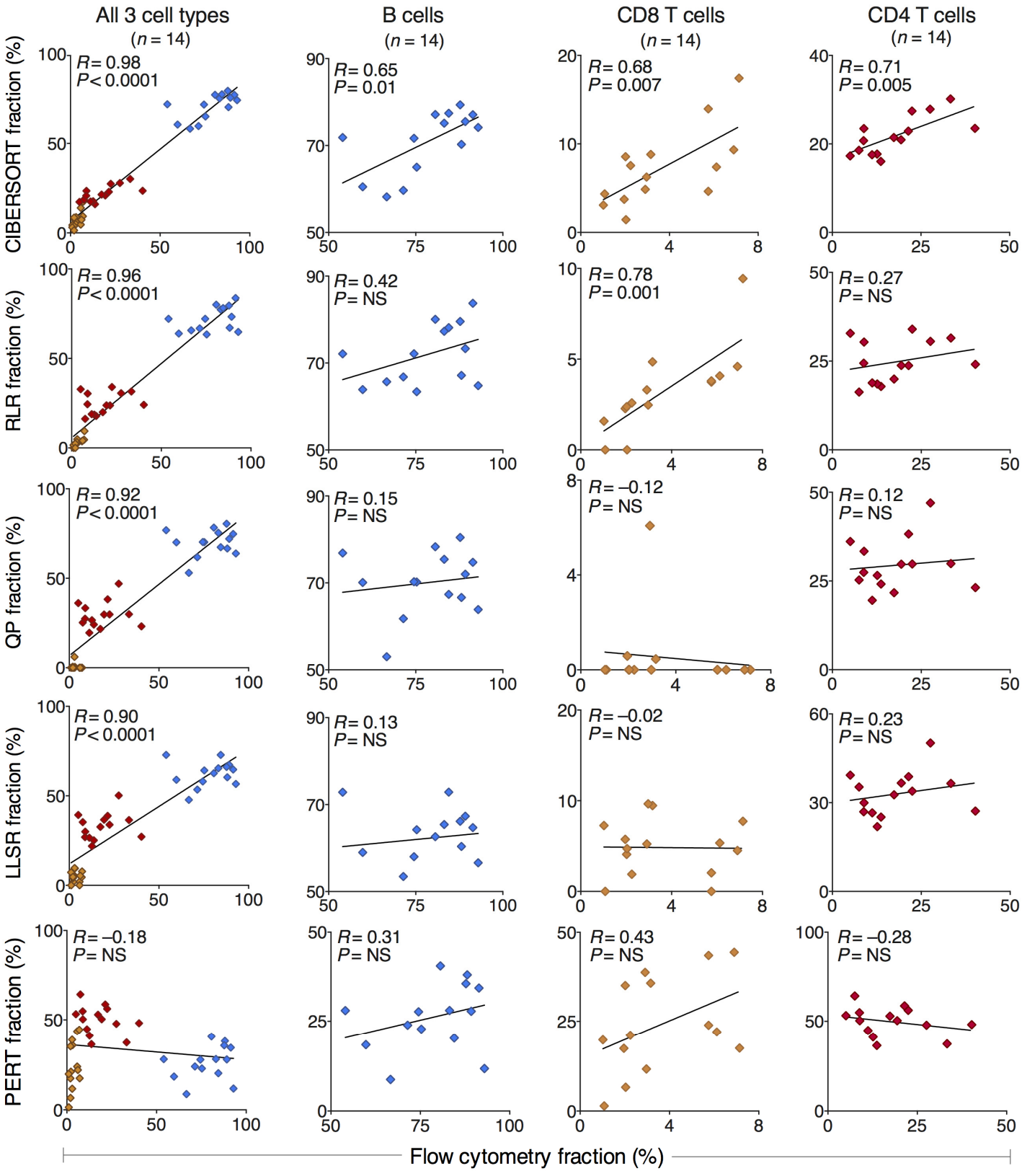

Supplementary Figure 13

Comparison of deconvolution methods for enumeration of three leukocyte subsets in FL tumor biopsies

Scatter plots comparing flow cytometry with five deconvolution methods for the enumeration of three leukocyte subsets, including malignant B cells, in disaggregated FL lymph node biopsies. For RMSE values of individual cell subsets, see **Supplementary Table 4**. Concordance between flow cytometry and GEP deconvolution was assessed by linear regression (solid lines). *R*, Pearson correlation.

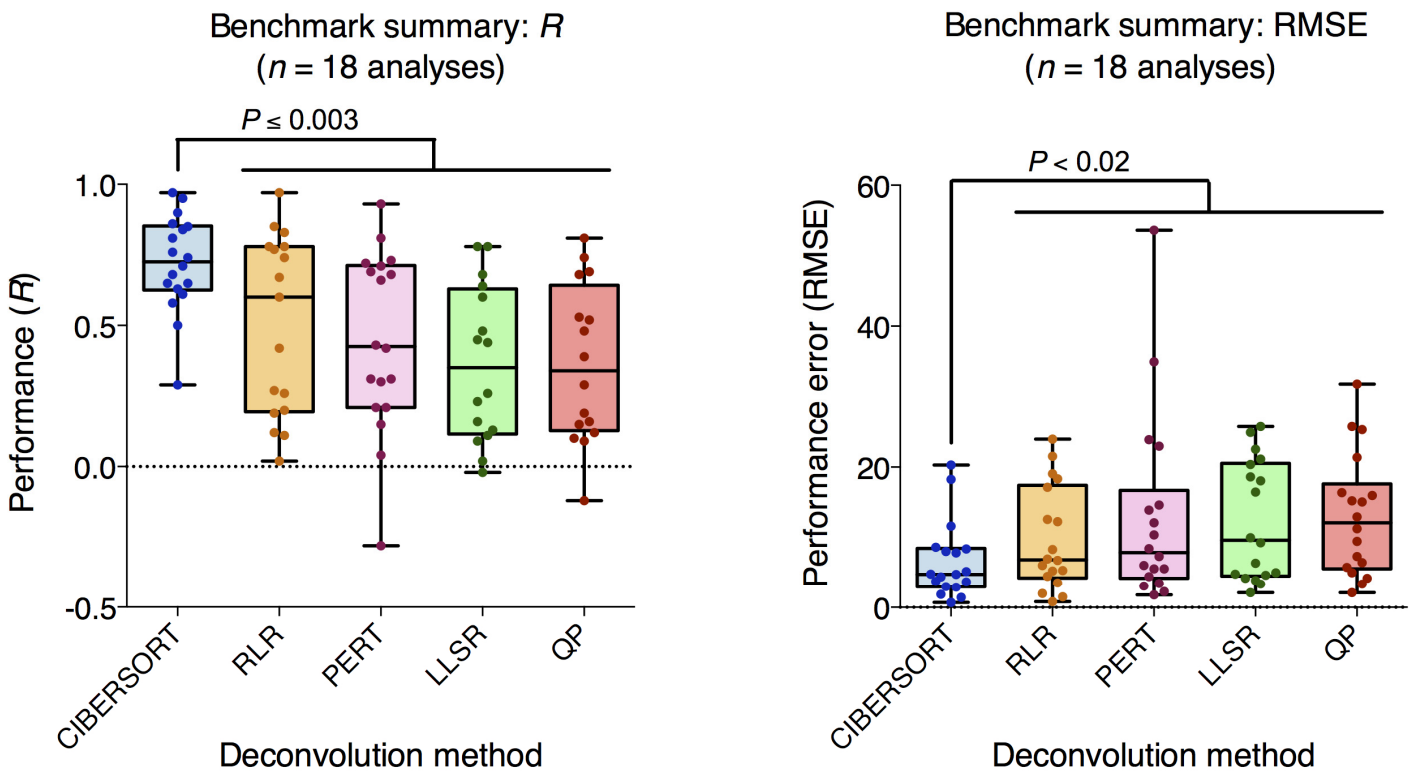

Supplementary Figure 14

Summary of benchmarking results for complex mixtures

Using two measures of performance (*R* and RMSE), CIBERSORT significantly outperformed other gene expression-based methods (paired two-sided Wilcoxon signed rank test), and generally performed better than all other methods on complex mixtures (**Fig. 2d**). Raw data are provided in 'Complex Mixtures' in **Supplementary Table 4**. For details of deconvolution methods, see Online Methods (also see **Supplementary Table 3** and **Supplementary Discussion**).

Supplementary Note

Flow cytometry. All panels are detailed below, with antibody clones indicated in brackets (all reagents were obtained from BD Biosciences). Panels used to evaluate deep deconvolution (**Fig. 3a**) were configured using lyophilized reagent plates (Lyoplates, BD Biosciences), with the exception of reagents in parentheses, which were added as liquid antibodies.

Fig.	Tissue	Panel	*n*	FITC	PE	PerCP-Cy5.5	PE-Cy7	APC	APC-H7	V450	A700	Pac-Blue	APC-Cy7	Alexa-647
S3b	Tonsils	T/B cell	5	CD5 [L17F12]	-	-	-	CD19 [HIB19]	-	-	-	-	-	-
2h	Normal lung tissue	Leukocyte	11	CD4 [OKT4]	CD14 [HCD14]	CD19 [HIB19]	CD56 [HCD56]	CD8 [SK1]	-	-	CD45 [HI30]	-	-	-
2i,3c	FL lymph nodes	T/B cell	14	CD8 [SK1]	-	-	-	-	-	-	-	CD4 [RPA-T4]	CD20 [L27]	-
3a	PBMCs 1	T cell	20	(CD85j) [GHI/75]	(CD28) [L293]	CD4 [SK3]	CD45RA [HI100]	CD27 [L128]	CD8 [SK1]	CD3 [UCHT1]	-	-	-	-
3a	PBMCs 1	Activated T cell	20	(TCRgd) [11F2]	(PD-1) [EH12.1]	CD4 [SK3]	CD38 [HB7]	HLA-DR [L243]	CD8 [SK1]	CD3 [UCHT1]	-	-	-	-
3a	PBMCs 1	B cell	20	IgD [IA6-2]	CD24 [ML5]	CD19 [SJ25C1]	CD38 [HB7]	CD27 [L128]	CD20 [2H7]	CD3 [UCHT1]	-	-	-	-
3a	PBMCs 1	CXCR3+	20	CD16+56 [3G8/NCAM16.2]	CXCR3 [1C6/CXCR3]	CD4 [SK3]	CD33 [P67.6]	CD19 [SJ25C1]	CD8 [SK1]	CD3 [UCHT1]	-	-	-	-
3b	PBMCs 2	Treg	7	-	CD4 [SK3]	-	-	-	-	-	-	CD3 [UCHT1]	-	FOXP3 [236A/E7]

For **Supplementary Fig. 3b**, tonsil-derived cell suspensions were thawed, washed, counted, and subsequently stained with monoclonal antibodies (above table) to label B cells ($CD19^+$) and T cells ($CD5^+$), without stimulation. Each population was sorted using a FACSAria II instrument (BD Biosciences) to >95% purity for subsequent expression profiling.

For **Fig. 2h**, fresh normal lung tissue samples were cut into small pieces and dissociated into single cell suspensions by 45 min of Collagenase I (STEMCELL Technologies) digestion. Dissociated single cells were suspended at 1×10^7 per mL in staining buffer (HBSS with 2% heat-inactivated fetal calf serum). After 10 min of blocking with 10 μg/μL rat IgG, the cells were stained for at least 10 min with the antibodies indicated in the above table. After washing, stained cells were re-suspended in staining buffer with 1 μg/mL DAPI, and the following populations were enumerated using a FACSAria II instrument (BD Biosciences): total leukocytes ($CD45^+$), monocytes ($CD14^+$), CD8 T cells ($CD8^+$), CD4 T cells ($CD4^+$), NK cells ($CD56^+$), and B cells ($CD19^+$).

For **Figs. 2i** and **3c** (and **Supplementary Fig. 13**), diagnostic FL tumor cell suspensions were stained with monoclonal antibodies (above table) to label CD4 T cells ($CD4^+$), CD8 T cells ($CD8^+$), and B cells ($CD20^+$). Stained cells were detected on a FACSCalibur or an LSR II 3-laser cytometer (BD Biosciences).

For **Fig. 3a** (and **Supplementary Fig. 12a**), flow cytometry phenotyping was performed on PBMCs from healthy adults using lyophilized reagent plates (Lyoplates, BD Biosciences). The plates were configured with staining cocktails shown in the above table to enumerate the following cell subsets: naïve B cells ($CD3^-CD19^+CD20^+CD24^-CD38^+$), memory B cells ($CD3^-CD19^+CD20^+CD24^+CD38^-$), CD8 T cells ($CD3^+CD8^+$), naïve CD4 T cells ($CD3^+CD4^+CD45RA^+CD27^+$), memory CD4 T cells ($CD3^+CD4^+CD45RA^-$), gamma delta T cells ($TCRgd^+$), NK cells ($CXCR3^+CD16^+CD56^+$), and monocytes (identified by size via forward- and side-scatter properties). Staining was performed according to the published protocol for Lyoplates on an LSRII flow cytometer (BD Biosciences)[1]. Reagents in parentheses in the above table were added as liquid antibodies, and were not part of the Lyoplate *per se*.

Finally, for the enumeration of regulatory T cells (Tregs) in **Fig. 3b** (and **Supplementary Fig. 12b**), peripheral blood was obtained from six healthy adult males by venipuncture into K2EDTA vacutainers (BD Biosciences) and processed immediately. Whole blood was diluted two-fold with PBS and mononuclear cells (PBMCs) isolated using Ficoll-Paque Plus (GE Healthcare). PBMCs were washed twice with PBS, counted, and 1×10^6 cells per individual, along with 1×10^6 cells from viably preserved PBMCs obtained from patient 4 in **Supplementary Fig. 4c**, were stained with αCD3, and αCD4 (see table above). Cells were washed in PBS, resuspended in Fix/Perm Buffer (eBiosciences), and incubated on ice for 20 min. Cells were washed twice in Perm/Wash Buffer (eBiosciences), and stained with αFOXP3. Cells were washed once in Perm/Wash Buffer and data collected using an LSRFortessa flow cytometer (BD Biosciences). Tregs were defined as $CD3^+CD4^+FOXP3^+$ non-doublet cells, and enumerated as a fraction of all intact PBMCs.

Low frequency leukocyte subsets in PBMCs. Related to the main text, the following five leukocyte subsets had low median fractions in PBMCs as determined by flow cytometry (<5%): naïve and memory B cells, activated memory CD4 T cells, gamma delta T cells, and Tregs.

Supplementary Results

Enumeration of activated and resting memory CD4 T cells by flow cytometry. Characteristic changes in gene expression accompany the phenotypic transition from naïve ($CDR45RA^{+}CD45RO^{-}$) to memory ($CD45RO^{+}CDR45RA^{-}$) T cells. Two such genes were profiled in our activated T cell panel (**Supplementary Notes**, above): HLA-DR, a canonical T cell activation marker primarily expressed on memory CD4 T cells[2,3] (as opposed to naïve subsets), and CD38, another known activation marker predominantly expressed on naïve CD4 T cells[3,4]. While our activation T cell panel did not include CD45RA or CD45RO, we confirmed previous findings by analyzing data from a separate study (data not shown), in which PBMCs were profiled using a panel that included αCD3, αCD4, αCD45RA, αHLA-DR and αCD38. Among $CD3^{+}CD4^{+}$ cells in 6 healthy subjects, we confirmed a strong correlation between total $HLA\text{-}DR^{+}$ cells and $HLA\text{-}DR^{+}CD45RA^{-}$ (activated memory) cells ($R = 0.97$, $P = 0.001$; RMSE = 0.7%). Conversely, total $HLA\text{-}DR^{-}CD38^{+}$ counts were significantly correlated with $HLA\text{-}DR^{-}CD38^{+}CD45RA^{+}$ (naïve) cells ($R = 0.87$; $P = 0.001$; RMSE = 11.9%), suggesting that the $CD3^{+}CD4^{+}HLA\text{-}DR^{+}$ phenotype represents a reasonable surrogate for activated memory CD4 T cells in healthy adult PBMCs. Therefore, to compare flow cytometry data with activated and resting memory CD4 subsets (from LM22) in this study, we used counts of $CD3^{+}CD4^{+}HLA\text{-}DR^{+}$ cells to estimate levels of activated memory CD4 T cells, and subtracted these values from total memory CD4 T cells ($CD3^{+}CD4^{+}CD45RA^{-}$) to estimate resting memory CD4 T cells.

Analysis of feature selection. A key aspect distinguishing CIBERSORT from previous methods is the context-dependent selection of genes from the signature matrix. This procedure increases CIBERSORT's tolerance to noise and prevents overfitting[5] (Online Methods). Based on the underlying framework of SVR, we hypothesized that genes with highly variable expression across a signature matrix *S*, or between *S* and a mixture *M*, would be selected most frequently (e.g., see **Supplementary Fig. 1**, Online Methods). On the other hand, if feature selection is more heavily determined by the specific cell subsets from *S* present in *M*, then marker genes of a cell type missing from *M* might be discarded, potentially impacting performance on cell types closely related to the missing cell type. To evaluate these hypotheses, we created a simple spike series of two uncorrelated reference profiles from LM22, including pure samples of each (resting mast cells and CD8 T cells) (**Supplementary Fig. 9a**). We reasoned that if SVR excludes marker genes when corresponding cell types in *S* are absent from *M*, then this behavior would be most apparent in pure samples of uncorrelated cell types. Therefore, we first compared genes selected by SVR for 100% resting mast cells, but not 100% CD8 T cells, and vice

versa, and tested for differences in expression. Interestingly, genes uniquely selected for CD8 T cells were more highly expressed in CD8 T cells compared to resting mast cells, however the difference in magnitude was modest and the converse was not observed for resting mast cells (**Supplementary Fig. 9b**). This suggests a possible enrichment for marker genes based on mixture content, but the relationship was inconsistent. We then extended our analysis to signature matrix genes selected in common between the two cell types, and found many genes with highly variable expression, both between the two cell types and across LM22 (data not shown). Notable examples include *CD8A* (CD8 T cell-enriched) and *CPA3* (mast cell carboxypeptidase A3), *CLC*, and *TPSAB1* (MC enriched). Separately, when examining the spike series, highly expressed genes across all LM22 cell subsets were frequently selected despite the fact that analyzed mixtures contained only CD8 T cells and resting mast cells (**Supplementary Fig. 9c**). This is consistent with our former hypothesis, and suggests that signature matrix genes for a cell type present in *S* but absent from *M* are not necessarily discarded; rather, they are likely useful to CIBERSORT by bounding the regression (e.g., *CD8A* was chosen regardless of whether CD8 T cells were present, likely informing their absence; see **Supplementary Fig. 1**, Online Methods).

Importantly, our observation was reproducible with highly correlated cell subsets (data not shown). For example, when LM22 was applied to a pure sample of naïve CD4 T cells, *CD8A* was selected, despite not being expressed by naïve CD4 T cells. Further, the five genes most highly expressed in naïve CD4 T cells in LM22 (*IL7R*, *CD3D*, *TRAC*, *LTB*, *TRBC1*) were selected, despite being among the top 10 most highly expressed genes in CD8 T cells and resting CD4 memory T cells (**Supplementary Table 1**). Since these genes are highly variable in LM22 (e.g., generally low or absent in myeloid subsets) these data are also consistent with our former hypothesis, and suggest that cell subsets missing from the mixture are unlikely to adversely impact deconvolution of closely related subsets in the mixture.

Supplementary Discussion

Review of gene expression deconvolution methods. A variety of GEP deconvolution methods have been proposed, many of which represent a gene expression admixture and its components as a linear equation, $\mathbf{m} = \mathbf{f} \times \mathbf{B}$, where **f** denotes a vector consisting of the unknown fractions of each cell type and **B** is a GEP signature matrix. Previous groups have applied linear least squares regression (LLSR)[6] and more recently, non-negative least squares regression (NNLS)[7] and quadratic programming (QP)[8-10] to solve for **f** (**Supplementary Table 3**). While LLSR provides a maximum likelihood solution for **f** under

a normally distributed error model, the solution is approximate and does not enforce non-negativity constraints (i.e., cell population levels should never be <0)[8]. Though suboptimal, this issue can be adequately addressed in practice by setting negative coefficients to zero, followed by normalizing remaining coefficients to sum to 1. By contrast, NNLS and QP can explicitly incorporate non-negativity constraints, and QP can produce a globally optimal solution to **f** (in a least-squares sense) in practical time[8].

LLSR, NNLS, and QP generally display good performance if (i) **B** is well conditioned (i.e., its component cell types are highly distinct) and (ii) **B** is applied to a mixture sample whose components are largely known (e.g., mature immune populations in peripheral blood)[6,8]. However, these methods have major limitations for complex tissue analysis. First, because all data in **m** and **B** are used to solve for **f**, these approaches are not robust to noise or outliers, and not ideal for mixtures with considerable unknown content (i.e., cell types not incorporated into the signature matrix). Of note, unlike QP and LLSR, methods based on robust linear regression (RLR) perform a feature selection prior to regression (like CIBERSORT) and are therefore more resilient to outliers (e.g., Huber M-estimator regression using rlm in R), which may lead to better performance on complex tissues. Second, LLSR, NNLS, and QP require a well-conditioned signature matrix, and may exhibit decreased performance on cell types with highly similar GEPs, such as CD8 versus CD4 T cells, or naïve versus memory B cells (e.g., **Fig. 3d**). Such GEPs may exhibit multicollinearity, and can lead to a 'winner takes all' phenomenon in which a higher weight would be assigned to the cell type whose GEP is most concordant with the mixture, whereas slightly less correlated cell types would be disproportionately down-weighted.

Recently, several new GEP deconvolution methods (PSEA[11], DSA[10], MMAD[12], PERT[7]) were introduced that can impute relative fractions of cell subsets in **m** (**Supplementary Table 3**). Like previous approaches, PSEA and DSA solve the same system of linear equations for **f** using LLSR or QP, respectively (see above). Unlike other methods, PSEA and DSA require cell type specific marker genes as input, rather than signatures matrices, limiting their scope to fewer cell types. Moreover, because DSA derives expression levels in **B** from the input (i.e., marker genes and a set of mixtures **M**) rather than prior knowledge, mixtures with unknown content or noise may lead to reduced performance (**Supplementary Figs. 5**, **6**). The other two methods, MMAD and PERT, employ more complicated models. The former attempts to correct for normalization bias in expression data, while the latter estimates a multiplicative perturbation constant that acts equally on all mixtures, representing either biologically meaningful perturbations from reference profiles (e.g., cell culture effects) or noise. Both

use conjugate gradient descent to maximize the likelihood of **f** given their respective model assumptions. While theoretically more robust than simpler models, in practice, we found both methods to be similarly susceptible to complex mixtures with unknown content and noise (**Supplementary Figs. 5**, **6** and **Supplementary Table 4**).

Some GEP deconvolution methods rely on grouped samples instead of single samples[7,10,12,13], and some of these methods estimate the basis profiles at the same time as the cell type proportions[10] and/or estimate group cell type-specific differences[12,13]. In so doing, most of these methods estimate cell type proportions in each sample[7,10,12], but in a manner that depends upon the combinations of mixtures analyzed (data not shown). Such methods may be less reliable for single sample deconvolution, a desirable feature for personalized applications[14].

Finally, while previous GEP deconvolution methods have been validated using 'ground truth' mixtures with known cell type proportions[6,8,11], no general metric has been proposed to estimate the 'goodness of fit' between deconvolution results and new mixture samples. In our view, such a filter is critically important before GEP deconvolution is adopted more widely.

Supplementary References

1. Maecker, H.T. et al. *BMC Immunol.* **6**, 13 (2005).
2. Johannisson, A. & Festin, R. *Cytometry* **19**, 343-352 (1995).
3. Kestens, L. et al. *Clin. Exp. Immunol.* **95**, 436-441 (1994).
4. Prince, H.E., York, J. & Jensen, E.R. *Cell. Immunol.* **145**, 254-262 (1992).
5. Cherkassky, V. & Ma, Y. *Neural Netw* **17**, 113-126 (2004).
6. Abbas, A.R., Wolslegel, K., Seshasayee, D., Modrusan, Z. & Clark, H.F. *PLoS One* **4**, e6098 (2009).
7. Qiao, W. et al. *PLoS Comput. Biol.* **8**, e1002838 (2012).
8. Gong, T. et al. *PLoS One* **6**, e27156 (2011).
9. Gong, T. & Szustakowski, J.D. *Bioinformatics* **29**, 1083-1085 (2013).
10. Zhong, Y., Wan, Y.-W., Pang, K., Chow, L. & Liu, Z. *BMC Bioinformatics* **14**, 89 (2013).
11. Kuhn, A., Thu, D., Waldvogel, H.J., Faull, R.L.M. & Luthi-Carter, R. *Nat. Methods* **8**, 945-947 (2011).
12. Liebner, D.A., Huang, K. & Parvin, J.D. *Bioinformatics* **30**, 682-689 (2014).
13. Shen-Orr, S.S. et al. *Nat. Methods* **7**, 287-289 (2010).
14. Shen-Orr, S.S. & Gaujoux, R. *Curr. Opin. Immunol.* **25**, 571-578 (2013).